Robust design optimization and stochastic performance analysis of a grid-connected photovoltaic system with battery storage and hydrogen storage

Diederik Coppitters[a,b,c,*], Ward De Paepe[a], Francesco Contino[d]

[a] *Thermal Engineering and Combustion Unit, University of Mons (UMONS), Place du parc 20, 7000 Mons, Belgium*
[b] *Fluid and Thermal Dynamics (FLOW), Vrije Universiteit Brussel, Pleinlaan 2, 1050 Brussels, Belgium*
[c] *Combustion and Robust Optimization Group (BURN), Vrije Universiteit Brussel (VUB) and Université Libre de Bruxelles (ULB), 1050 Brussels, Belgium*
[d] *Institute of Mechanics, Materials and Civil Engineering (iMMC), Université catholique de Louvain (UCLouvain), Place du Levant, 2, 1348 Louvain-la-Neuve*

Abstract

Balancing of intermittent energy such as solar energy can be achieved by batteries and hydrogen-based storage. However, combining these systems received limited attention in a grid-connected framework and its design optimization is often performed assuming fixed parameters. Hence, such optimization induces designs highly sensitive to real-world uncertainties, resulting in a drastic mismatch between simulated and actual performances. To fill the research gap on design optimization of grid-connected, hydrogen-based renewable energy systems, we performed a computationally efficient robust design optimization under different scenarios and compared the stochastic performance based on the corresponding cumulative density functions. This paper provides the optimized stochastic designs and the advantage of each design based on the financial flexibility of the system owner. The results illustrate that the economically preferred solution is a photovoltaic array when the self-sufficiency ratio is irrelevant ($\leq 30\,\%$). When a higher self-sufficiency ratio threshold is of interest, i.e. up to $59\,\%$, photovoltaic-battery designs and photovoltaic-battery-hydrogen designs

*Corresponding author
Email address: diederik.coppitters@umons.ac.be (Diederik Coppitters)

provide the cost-competitive alternatives which are least-sensitive to real-world uncertainty. Conclusively, including storage systems improves the probability of attaining an affordable levelized cost of electricity over the system lifetime. Future work will focus on the integration of the heat demand.

Keywords: Grid-connected demand, Hydrogen storage, Levelized Cost Of Electricity, Photovoltaic, Robust design optimization, Uncertainty Quantification.

1. Introduction

With an expected increase of 575 GW between 2018 and 2023, solar PhotoVoltaic (PV) systems dominate the renewable capacity growth [1]. Despite this expected capacity expansion, PV systems are unable to cover the entire electricity demand, due to the intermittent behavior of solar energy. To address this intermittency, the addition of an electrical energy storage system enables to store an excess of solar energy and to reproduce this energy when electricity demand exceeds PV production. For such intermittent balancing, battery energy storage and hydrogen energy storage provide a flexible, adequate solution [2]. Battery storage achieves a fast response time and a high round-trip efficiency ($\approx 80\%$, as opposed to $\approx 35\%$ for hydrogen storage), which makes it suitable for short-term energy storage (i.e. from seconds to days) [2]. Nevertheless, due to their self-discharge rate and low energy density (30 Wh /kg), batteries are suboptimal for long-term energy storage (i.e. from weeks to months) [3]. Instead, hydrogen storage is suggested for seasonal energy storage, as hydrogen storage operates with a negligible discharge rate, achieves a higher energy density (up to 10 kWh /kg) and provides a flexible capacity setting of power charging, energy storage and power discharging [2, 3]. In this framework, power charging is generally performed by splitting water into hydrogen and oxygen in a Proton Exchange Membrane (PEM) electrolyzer [4], because of its fast response time (< 1 s) and full load flexibility [5]. The reverse reaction is generally performed in a PEM fuel cell to discharge the power [6]. The PEM fuel cell technology

Nomenclature

A	area, m^2
C	capacity, Ah
CAPEX	specific capital expense, €/kW
$CAPEX_a$	annual capital expense, €
d	stochastic dimension
E	electric energy, MWh
f	inflation rate, %
f_w	fraction of wholesale electricity price to retail electricity price, %
F	Faraday constant, 96 485 C/mol
G	annual solar irradiance variation, %
$G_{c,a}$	annual grid cost, €
HRES	Hybrid Renewable Energy System
i'	nominal interest rate, %
I	current, A
LCOE	Levelized Cost Of Electricity, €/MWh
n	component lifetime, h
N_{bat}	battery stack capacity, kWh
N_{elec}	electrolyzer array capacity, kW
N_{FC}	fuel cell array capacity, kW
N_{PV}	photovoltaic array capacity, kW_p
N_{tank}	hydrogen tank capacity, MWh
OPEX	specific operational expense, €/kW
$OPEX_a$	annual operational expense, €
p	pressure, Pa
PEM	Proton Exchange Membrane
PV	PhotoVoltaic
R	resistance, Ω
$R_{c,a}$	annual replacement costs, €
RDO	Robust Design Optimization
SOC	State Of Charge
SSR	Self Sufficiency Ratio, %
T	temperature, K
U	voltage, V
UQ	Uncertainty Quantification
w	wholesale electricity price, €/MWh
η	efficiency
μ	mean
ξ	independent random parameter
σ	standard deviation
Ψ	orthogonal polynomial
amb	ambient
an	anode
bat	battery
cat	cathode
ch	charge
dch	discharge
el	electric
elec	electrolyzer
FC	fuel cell
L	photogenerated
mem	membrane
nom	nominal
oc	open-circuit
pl	bipolar plates
sh	shunt
s	series
th	thermal

is widespread commercially, it operates at low temperature (70 °C- 100 °C) and achieves high power densities (up to 2 W/cm^2) [7].

Design optimization studies on standalone Hybrid Renewable Energy Systems (HRES) including battery storage and hydrogen storage are well-established [8]. Han et al. described a mode-triggered droop scheme for an islanded PV-battery-hydrogen DC microgrid and showed that combining hydrogen storage and battery storage provides stronger environmental adaptability and higher PV utilization [9]. Khiareddine et al. performed a design optimization of a stand-alone PV-wind-battery-hydrogen system and concluded that an adequately sized fuel cell array allows a significant reduction in battery capacity and thus reduction of the total cost [10]. Zhang et al. evaluated different configurations of a stand-alone PV-wind-battery-hydrogen system and concluded that battery storage is the most cost-effective solution, while hydrogen storage is a reliable and non-polluting alternative, which can become economically advantageous after cost and efficiency improvements [11]. Recently, also design optimization studies on grid-connected Hybrid Renewable Energy Systems (HRES) including battery storage and hydrogen storage received attention. Parra et al. illustrated the increase in on-site energy production of a PV-powered, grid-connected dwelling by considering battery and hydrogen storage, resulting in an additional annual income of £112 and £102, respectively [12]. Pellow et al. compared battery storage and hydrogen storage for grid-connected systems and conclude that hydrogen storage achieves a higher electrical Energy Stored On Invested than battery storage [13]. Zhang et al. optimized a grid-connected PV-battery-hydrogen system, considering several operation strategies and two different cost scenarios [3]. Under the optimistic cost scenario, hydrogen storage induces a higher Net Present Value. Despite the clear advantage of this type of HRES, Eriksson et al. highlighted that incorporating hydrogen in HRES design optimization is still an anomaly: only 5 out of 30 surveyed HRES studies incorporated hydrogen-based energy systems [14].

During model-based HRES design optimization studies, deterministic model parameters are assumed (i.e. perfectly known and free from inherent variations).

However, the HRES performance is mainly characterized by parameters subject to uncertainty (e.g. stochastic nature of solar energy, operation and maintenance costs, operating temperature) [15]. Moreover, in the hydrogen market, it remains a big challenge to obtain real market values [16]. Consequently, the uncertainty on these parameters affects the HRES performance, leading to a stochastic behavior of the system objectives. The state-of-the-art method that propagates parameter uncertainties through a system model and quantifies the statistical moments of the model output (i.e. Uncertainty Quantification (UQ)) is Monte Carlo Simulation [17]. This method is a robust (i.e. always converging) and easy-to-implement technique, but it requires a significant number of model evaluations ($10^4 - 10^5$) to attain an acceptable level of convergence on the statistical moments. Computationally-efficient alternatives are surrogate model construction methods, such as Gaussian Process Regression [18] and Polynomial Chaos Expansion (PCE) [19]. During the post-process of the surrogate model (i.e. quantification of the statistical moments), PCE provides significant advantages, such as the analytic quantification of the statistical moments and the Sobol' indices out of the PCE coefficients [20].

When the mean and standard deviation of a model output can be quantified efficiently, these statistical moments can be used as optimization objectives. Through a multi-objective optimization algorithm, a Pareto set of optimized designs can be found that makes a trade-off between minimizing the output mean and minimizing the output standard deviation (i.e. Robust Design Optimization (RDO)). The design leading to the minimum standard deviation on the model output (i.e. the robust design) is least-sensitive to the parameter uncertainties and therefore provides the most resilient performance. In the framework of RDO, the Taguchi methodology quantifies the mean square deviation of several designs subject to noise [21]. A gradual setting of worst-case scenario-based design optimization aims to minimize the loss in objective function by considering least favorable conditions (i.e. min-max optimization) [22]. In surrogate-assisted RDO, the output mean and output standard deviation for every design sample are quantified via a surrogate modelling method [23].

In design optimization studies of HRES, the optimal integration of battery systems and hydrogen-based energy systems in grid-connected applications received limited attention. Moreover, the model parameters are often assumed fixed and free from inherent variations, while the rare consideration of uncertainty is limited to linear models and only a handful of uncertain parameters (< 5), characterized by generic ranges based on assumptions [24]. Akbari et al. evaluated a distributed energy system, subject to a general variability of $\pm 20\,\%$ for a handful of financial parameters and demand parameters [25]. Parisio et al. considered the converter efficiencies related to electricity and heat demand to be uncertain between a general range of $\pm 10\,\%$ on a linear model of an energy hub [26]. These linear models are subject to large inherent uncertainty, while the variation of other highly-uncertain parameters (e.g. investment cost, lifetime) during real-world design, planning and operation is ignored. Moreover, generic variability ranges assume equal weights for every uncertainty, which leads to biased results. Combined, these assumptions bring forward designs that are highly sensitive to real-world uncertainties and result in a drastic mismatch between simulated and actual performances. To fill the research gap on design optimization under uncertainty of grid-connected, HRES including hydrogen storage and battery storage, we provide the following main contributions: the significant techno-economic uncertain parameters are characterized by their uncertainty as described in literature; to handle this large stochastic dimension, the advantages of the sparse PCE algorithm developed by Abraham et al. are exploited for the first time in a surrogate-assisted RDO algorithm [27]; the Cumulative Density Functions (CDF) of the optimized designs are used to compare the respective stochastic performances, which provides new insights into the probability of attaining an affordable levelized cost of electricity when combining battery storage and hydrogen storage with a PV array.

In this paper, the HRES model and the RDO method are described in section 2. The optimized designs for every demand type and their stochastic performance are presented in section 3. Conclusively, section 4 illustrates the main conclusions of this work, while the appendix consists of the detailed dataset and

convergence curves of the sparse PCE method.

2. Method

This section introduces the HRES, followed by the Python-based component models and the quantities of interest. Thereafter, the uncertainty characterization is described and the method to propagate the uncertainties through the model is presented. Finally, the RDO algorithm is illustrated.

2.1. Hybrid Renewable Energy System model

The considered system is a grid-connected load, supported by an HRES (Figure 1). The HRES consists of a PV array, which is coupled to a DC bus bar through a DC-DC converter with Maximum Power Point Tracking. A battery stack and electrolyzer array with storage tank are integrated to store the excess of PV array electricity. A fuel cell array is implemented to produce electricity from the stored hydrogen. To transfer the DC electricity from the battery system and fuel cell to the AC load, a DC-AC converter is connected.

To set the hierarchy between the subsystems, a typical power management strategy is implemented, which primarily aims to satisfy the demand [28]. In this strategy, excess PV power is supplied to the battery stack. When the determined charge current violates the maximum charge current, the nominal charge current is considered instead. Then, or when the battery array reaches its maximum State Of Charge (SOC), the surplus energy is used to power the electrolyzer array. When the hydrogen tank is full, or when the surplus power lies outside the electrolyzer array operating range, the surplus energy is sold to the grid at the wholesale electricity price.

In the opposite case, when the PV array does not cover the demand, the remaining demand is covered by the battery array, if the discharge current does not violate the maximum discharge current and the SOC remains above the SOC lower limit. If not, nominal discharge current is extracted and the additional power is supplied by the fuel cell array. When insufficient, the grid covers the remaining demand.

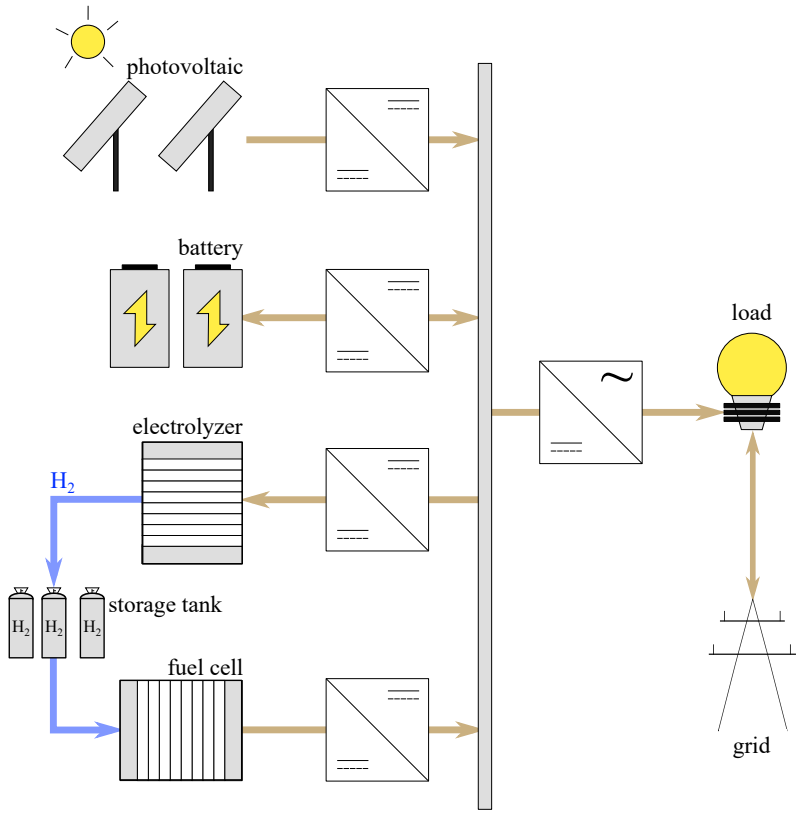

Figure 1: The considered system includes the load connected to the grid and supported by a Hybrid Renewable Energy System (HRES). This HRES consists of a PhotoVoltaic (PV) array which converts solar energy into electricity. The battery stack and hydrogen-based energy system (electrolyzer, fuel cell and storage tank) enable the system to store an excess of PV array electricity and to comply, up to the available energy, with the demand when the solar irradiance is insufficient.

2.1.1. Photovoltaic array

To determine the electricity produced by a PV array, we imported the experimentally-validated model out of the PVlib Python library [29]. The model quantifies the PV panel current-voltage characteristic through the following single-diode equation:

$$I_{\mathrm{PV}} = I_{\mathrm{L}} - I_0 \left(\exp\left(\frac{U + I R_{\mathrm{s}}}{n_{\mathrm{diode}} N_{\mathrm{s}} U_{\mathrm{th}}} \right) - 1 \right) - \frac{U + I R_{\mathrm{s}}}{R_{\mathrm{sh}}}. \tag{1}$$

The parameters in Equation 1 are not provided by the PV manufacturer. Therefore, we adopted the method by De Soto et al. to determine these parameters out of manufacturer data [30].

2.1.2. Battery stack

Lead-acid battery technology is selected in this work, as it is the most widespread technology and a mature lead-acid battery industry exists with significant learning rates during the last decades [31]. To characterize the performance of a lead-acid battery stack, we adopted the experimentally-validated model of Blaifi et al. [32]. The general voltage-current relation for a lead-acid battery is defined as:

$$U_{\mathrm{bat}} = U_{\mathrm{bat,oc}} + I_{\mathrm{bat}} R_{\mathrm{bat}}, \tag{2}$$

where the current I_{bat} is positive during charge and negative during discharge. The resistance component R_{bat} is different during charge and discharge and depends on the temperature, the current magnitude and the capacity. Hence, the characterization of the voltage during charge and discharge is given by:

$$U_{\mathrm{ch}} = (2.085 - 0.12\,(1 - \mathrm{SOC})) - \frac{I}{C_{\mathrm{nom}}} \left(\frac{4}{1 + I^{1.3}} + \frac{0.27}{\mathrm{SOC}^{1.5}} + 0.02 \right) (1 - 0.007 \Delta T)\,, \tag{3}$$

$$U_{\mathrm{dch}} = (2 - 0.16\ \mathrm{SOC}) + \frac{I}{C_{\mathrm{nom}}} \left(\frac{6}{1 + I^{0.86}} + \frac{0.48}{(1 - \mathrm{SOC})^{1.2}} + 0.036 \right) (1 - 0.025 \Delta T)\,. \tag{4}$$

The State Of Charge (SOC) is the fraction of the total capacity stored in the battery:

$$\mathrm{SOC}\,(t) = \mathrm{SOC}_0 + \frac{1}{C\,(t)} \int_0^t \eta_{\mathrm{bat}}\,(t)\, I\,(t)\, \mathrm{d}t, \tag{5}$$

In this work, the minimum SOC is set at 20 % [33, 34].

We estimated the lifetime based on SOC variations through the commonly implemented Rainflow cycles counting method [35]. To avoid excessive reduction

of the lifetime, overcharging and over discharging are avoided, while the maximum charge current and maximum discharge current are limited to $C_{\mathrm{nom}}/10$ and $C_{\mathrm{nom}}/3.3$, respectively [36]. Because of the constraints limiting the operation in the optimal operating zone to prolong battery life, we assumed a yearly capacity degradation rate [37] and a fixed energy efficiency of 80 % [38].

2.1.3. Electrolyzer array

To determine the voltage-current characteristic and hydrogen flow rate of the PEM electrolyzer array, we selected the experimentally-validated model from Abdin et al. and we consider an operating pressure of 30 bar [39]. The operating voltage is characterized according to the following equation:

$$U_{\mathrm{elec}} = U_{\mathrm{elec,oc}} - U_{\mathrm{elec,act}} - U_{\mathrm{elec,ohm}} - U_{\mathrm{elec,con}}. \tag{6}$$

In the remainder of this subsection, the subscript "elec", which refers to "electrolyzer", is left out for ease of reading. The open-circuit voltage follows out of the Nernst equation for electrolysis:

$$U_{\mathrm{oc}} = \left(1.229 - 0.9 \times 10^{-3}\,(T - 298)\right) + \frac{R_{\mathrm{u}}T}{2F}\left(\ln\left(\frac{p_{\mathrm{H_2}}\sqrt{p_{\mathrm{O_2}}}}{a_{\mathrm{H_2O}}}\right)\right), \tag{7}$$

where R_{u}, F and a represent the universal gas constant, Faraday constant and water activity between electrode and membrane, respectively. The activation overpotential U_{act} represents the voltage used to transfer electrons between the electrodes. By inverting the Butler-Volmer equation for the reactions at the electrode surface, the activation voltage can be quantified:

$$U_{\mathrm{act}} = \frac{R_{\mathrm{u}}T}{\alpha_{\mathrm{an}}F}\mathrm{arcsinh}\left(\frac{i}{2i_{0,\mathrm{an}}}\right) + \frac{R_{\mathrm{u}}T}{\alpha_{\mathrm{cat}}F}\mathrm{arcsinh}\left(\frac{i}{2i_{0,\mathrm{cat}}}\right). \tag{8}$$

At high currents, a concentration overpotential U_{con} is created due to an excess of reactants (e.g. oxygen bubbles slowing down the reaction). To quantify this overpotential, a combination of the Nernst equation and Fick's law is adopted:

$$U_{\mathrm{con}} = \frac{R_{\mathrm{u}}T}{4F}\ln\frac{C^{\mathrm{mem}}_{\mathrm{O_2}}}{C^{\mathrm{mem}}_{\mathrm{O_2},0}} + \frac{R_{\mathrm{u}}T}{2F}\ln\frac{C^{\mathrm{mem}}_{\mathrm{H_2}}}{C^{\mathrm{mem}}_{\mathrm{H_2},0}}, \tag{9}$$

where C^{mem} is the concentration at the membrane-electrode interface, and the subscript 0 refers to the reference working condition. The final overpotential that occurs in the PEM electrolyzer is the ohmic overpotential U_{ohm}, which is driven by the electric resistance of the electrodes R_{el}, bipolar plates R_{pl} and the membrane R_{mem}:

$$U_{\mathrm{ohm}} = I\left(R_{\mathrm{el}} + R_{\mathrm{pl}} + R_{\mathrm{mem}}\right). \tag{10}$$

The electric resistance of the electrodes and the flow plates can be quantified by applying Ohms law. We refer to Abdin et al. for further details on the determination of the overpotentials [39]. Finally, following the working point of the electrolyzer array, the hydrogen molar flow rate $n_{\mathrm{H_2}}$ is formulated as:

$$n_{\mathrm{H_2}} = \frac{I}{2F}. \tag{11}$$

Despite the effect of intermittent loading on degradation and lifetime is not yet well quantified, this effect is reported to be negligible by several manufacturers [5]. Therefore, this effect is not considered in this study and a fixed degradation rate per operating hour is assumed.

2.1.4. Hydrogen storage tank

The pressurized hydrogen produced in the electrolyzer is stored in a storage tank. Filling up the storage tank increases the tank pressure, until the electrolyzer outlet pressure is reached, according to the ideal gas law [40]:

$$p_{\mathrm{t}} - p_{\mathrm{t,init}} = Z\frac{N_{\mathrm{H_2}} R_{\mathrm{u}} T_{\mathrm{t}}}{M_{\mathrm{H_2}} V_{\mathrm{t}}}. \tag{12}$$

The compressibility factor Z for H_2 is equal to 1 at room temperature and moderate pressure ($< 100\,\mathrm{bar}$) [40].

2.1.5. Fuel cell array

To represent the conversion of hydrogen and oxygen into water in a PEM fuel cell array, we adopted the model from Murugesan et al. which is experimentally

validated on the Ballard-Mark-V PEM fuel cell [41]. The operating current depends on the converted hydrogen molar flow rate:

$$I_{\mathrm{FC}} = 2Fn_{\mathrm{FC,H_2}}. \tag{13}$$

The electric potential produced during water composition out of hydrogen and oxygen is equal to the Nernst potential minus the losses:

$$U_{\mathrm{FC}} = U_{\mathrm{FC,Nernst}} - U_{\mathrm{FC,act}} - U_{\mathrm{FC,ohm}} - U_{\mathrm{FC,con}}. \tag{14}$$

In the remainder of this subsection, the subscript "FC" is left out for ease of reading. The Nernst equation determines the maximum fuel cell voltage and considers the operating temperature and reactant pressures:

$$U_{\mathrm{Nernst}} = 1.229 - 0.85 \times 10^{-3}(T - 298.15) + 4.31 \times 10^{-5} T \left(\ln\left(p_{\mathrm{H_2}}\right) + 0.5 \ln\left(p_{\mathrm{O_2}}\right)\right). \tag{15}$$

The activation losses U_{act} occur due to a low rate of charge transfer at lower current densities. This activation loss corresponds to:

$$U_{\mathrm{act}} = -0.948 + 0.00354T + 7.6 \times 10^{-5} T \ln\left(C_{\mathrm{O_2}}\right) + -1.93 \times 10^{-4} T \ln\left(I\right). \tag{16}$$

The ohmic losses U_{ohm} occur out of electrolyte resistance, contact resistance at the collector plates and at the graphite electrodes. This loss is linearly dependent to the load:

$$U_{\mathrm{ohm}} = iR_{\mathrm{ohm}} = i\frac{\delta_{\mathrm{mem}}}{\sigma_{\mathrm{mem}}}, \tag{17}$$

where R_{ohm} is the electrical resistance that depends on the membrane thickness δ_{mem} and membrane conductivity σ_{mem} (Nafion 117). The concentration loss occurs due to changes in concentration of reactants at higher current density region:

$$U_{\mathrm{con}} = -0.016 \ln\left(1 - \frac{i}{i_{\mathrm{lim}}}\right). \tag{18}$$

We refer to the work of Murugesan et al. for the detailed quantification of these losses [41]. Similar to the PEM electrolyzer, the effect of intermittent operation on the degradation and lifetime is not yet fully understood [42]. Therefore, a fixed degradation rate per operating hour is assumed.

2.1.6. Power conversion

The components are connected to a DC bus bar through DC-DC converters. To provide the power to the load or the grid, the DC bus bar is connected through a DC-AC inverter. The conversion efficiency of a DC-DC converter η_{conv} depends on the component output power:

$$P_{\text{DC,out}} = \eta_{\text{conv}}\left(P_{\text{DC,out}}\right) P_{\text{DC,in}}. \tag{19}$$

The conversion efficiency depends on the converter type. We considered the experimentally buck-boost converter efficiency profile presented by Taghvaee et al. for the PV array, PEM electrolyzer array and fuel cell array and a bidirectional buck-boost converter efficiency profile for the battery stack [43]. Similar to the DC-DC converter, the DC-AC inverter efficiency profile η_{inv} depends on the AC output power $P_{\text{AC,out}}$:

$$P_{\text{AC,out}} = \eta_{\text{inv}}\left(P_{\text{AC,out}}\right) P_{\text{DC,in}}. \tag{20}$$

In this work, the inverter efficiency profile is determined by the experimentally-validated method described by Rampinelli et al. [44].

2.2. Climate and demand data

The HRES performance depends on the climate and demand characteristics. In this work, we evaluated a dwelling and a community (i.e. 2500 dwellings) in Brussels, Belgium (Figure 2). When adopting climate data and demand data, it is important to adopt the climate data that was used to generate the demand data, as the solar irradiance and ambient temperature affect how the demand behaves. Therefore, we appeal to Typical Meteorological Year data and hourly demand data from the National Renewable Energy Laboratory, as the former is

used to construct the latter [45, 46]. As the data only exists for locations in the United States of America, we applied the method presented by Montero Carrero et al. to adapt the climate and demand profiles for Belgium [47].

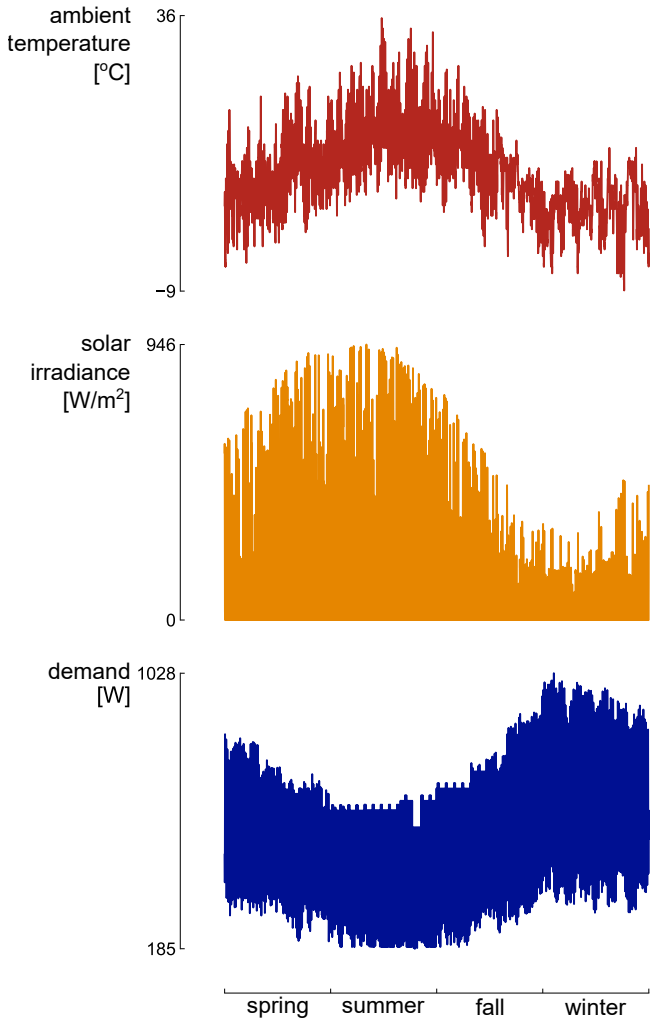

Figure 2: The climate data (solar irradiance and ambient temperature) and demand data are inversely proportional, resulting in a reduced demand during spring and summer and a peak demand during fall and winter.

2.3. Performance indicators

To evaluate the techno-economic performance of the HRES, the Levelized Cost Of Electricity (LCOE) is selected. The LCOE of the hybrid system reflects the system cost per unit of electricity covered [33]:

$$\mathrm{LCOE} = \frac{\mathrm{CAPEX_a} + \mathrm{OPEX_a} + R_{\mathrm{c,a}} + G_{\mathrm{c,a}} - G_{\mathrm{s,a}}}{\sum_{i=0}^{8760} P_{\mathrm{load}}}. \tag{21}$$

To determine the system cost, the annualized investment cost $\mathrm{CAPEX_a}$, operational cost $\mathrm{OPEX_a}$, replacement cost $R_{\mathrm{c,a}}$, grid electricity cost $G_{\mathrm{c,a}}$ and the gain from selling excess electricity $G_{\mathrm{s,a}}$ are evaluated. We refer to Zakeri et al. for the detailed quantification of these parameters [33]. The specific cost parameters values are listed in Table A.3.

To indicate the fraction of the load that is covered by the HRES, the Self-Sufficiency Ratio (SSR) is quantified as a secondary performance indicator [3]:

$$\mathrm{SSR} = 1 - \frac{E_{\mathrm{grid}}}{E_{\mathrm{load}}}, \tag{22}$$

where E_{load} is the total energy demand over the system lifetime. The SSR is an important factor for adopters of HRES, as it illustrates the resilience against large electricity price increases and the protection against power cuts, which are more likely in the future [48]. Moreover, reaching a significant SSR threshold is beneficial for grid operators, as it reduces the simultaneous power extraction from the grid and therefore reduces the risk of black-outs.

2.4. Uncertainty characterization

To represent the uncertainty during design and operation of the HRES, the model parameters are characterized by a uniform distribution based on literature (Table A.3). During operation, the system is subject to natural variability of the technical parameters, e.g. fluctuating operating temperature and pressure, varying degradation speed and an uncertain component lifetime. Additionally, inter-annual variability is present on the electricity demand, solar irradiance and ambient temperature [15]. From an economic point of view, the system is

subject to commissioning and maintenance quality, which affects the operating and maintenance cost, uncertain replacement cost due to evolving market conditions and a highly-uncertain wholesale electricity price due to an evolving energy mix, improved energy efficiency and increased electrification of fossil-based energy sectors [49]. Otherwise, the interest rate and the investment cost can be considered deterministic or uncertain, depending on the actual step of the design process and the finance type considered [15]. Most studies assume a single-stage investment at the project start, which implies a deterministic characterization of these parameters. However, a change in the finance type of the project and a significant timeframe between the design stage and investment stage, which increases the possibility for the market conditions to change between the stages, implies uncertainty on the interest rate and investment costs. Therefore, in this work, two scenarios are assumed. The first scenario considers the interest rate and investment costs as deterministic (i.e. fixed market conditions), while the second scenario treats these parameters as uncertain (i.e. varying market conditions). As the results are significantly influenced by the design step and investment type, the handling of two scenarios enables to compare with both commonly adopted scenarios in scientific literature.

2.5. Uncertainty Quantification

Following the computational cost of the model evaluation ($\approx 150\,\mathrm{s}$) and the large number of uncertainties considered (36 in the variable market conditions scenario and 28 in the fixed market conditions scenario), we considered a computationally efficient sparse Polynomial Chaos Expansion (PCE) method to propagate the uncertainty and quantify the statistical moments of the HRES performance indicators [27]. The PCE representation of the system model consists of a series of orthogonal polynomials Ψ_i with corresponding coefficients u_i:

$$\hat{M}(\boldsymbol{\xi}) = \sum_{i=0}^{P} u_i \Psi_i(\boldsymbol{\xi}) \approx M(\boldsymbol{\xi}), \tag{23}$$

where $\boldsymbol{\xi} = (\xi_1, \xi_2, ..., \xi_d)$ represents a vector of independent random parameters, d is the stochastic dimension and $P + 1$ equals the number of terms in the truncated series, determined by the polynomials up to a certain degree p for the considered stochastic dimension d:

$$P + 1 = \frac{(p + d)!}{p!d!}. \tag{24}$$

The number of terms in the truncated series increases dramatically when $d > 10$ (i.e. *curse-of-dimensionality*) [50]. Therefore, we adopted the sparse PCE algorithm developed in our research group which includes only the most significant coefficients (and corresponding polynomials) in the truncated series [27]. To determine the significant coefficients a priori, the algorithm first creates an initial design of experiments $\chi = [\boldsymbol{\xi}^1, \boldsymbol{\xi}^2, ..., \boldsymbol{\xi}^n]$, which are evaluated through the system model. In the first forward step of the algorithm, $P + 1$ one-predictor surrogate models are created and assessed individually by fitting their response with the output of the system model evaluations. Each one-predictor model and the variance of the coefficient are determined through the Least-Square Minimization method. The best performing one-predictor model (i.e. the most significant coefficient and corresponding orthogonal polynomial) is stored in the final regression model and the polynomial is removed from the pool of basis functions. This process is repeated until the maximum number of iterations is reached. Additional details on this sparse PCE method are described by Abraham et al. [27].

When the coefficients are quantified, the mean μ, standard deviation σ and Sobol' indices follow analytically through post-processing of the coefficients (i.e. no additional model evaluations required). The total-order Sobol' indices ($S_i^{T,\mathrm{PC}}$) quantify the total impact of a stochastic input parameter on the performance indicator, including all interactions:

$$S_i^{T,\mathrm{PC}} = \sum_{\alpha \in A_i^T} u_\alpha^2 / \sum_{i=1}^{P} u_i^2 \qquad A_i^T = \{\alpha \in A | \alpha_i > 0\}, \tag{25}$$

where A is the set of all the PCE coefficients and α_i represents the coefficient

related to uncertain parameter i.

In this work, a polynomial order of 3 is required to approximate the real model behavior accurately ($< 1\,\%$ error on the statistical moments, compared to a Monte Carlo Simulation result). The sparse PCE method achieves similar accuracy to the full PCE with only 29 % of the required model evaluations (Figure A.9), leading to a significant increase in computational efficiency of the method.

2.6. Surrogate-assisted Robust Design Optimization

The surrogate-assisted RDO aims at finding an optimized design (or set of optimized designs) which minimizes the LCOE mean and minimizes the LCOE standard deviation. The LCOE mean indicates the average expected LCOE over the system lifetime and should, therefore, be minimized to foresee a cost-competitive design. However, the LCOE standard deviation indicates the uncertainty on that expected mean LCOE. Reducing the LCOE standard deviation decreases the sensitivity to the uncertain environment, which increases the probability of operating near that LCOE mean in reality. To be able to find the designs that minimize these objectives, the capacity of the PV array, battery stack, PEM electrolyzer array, PEM fuel cell array and storage tank are selected as continuous design parameters. By considering the capacities as independent design parameters, the optimization algorithm can exclude any technology from the HRES. Due to the complexity and non-linearity of the HRES, the Non-dominated Sorting Genetic Algorithm (NSGA-II) is selected as an optimization algorithm [51, 52]. The algorithm creates and evaluates an initial population of design samples. As the mean and standard deviation of the LCOE are required to evaluate the population, the sparse PCE method is applied to the HRES model for each design sample. Once the statistical moments on the LCOE for the population are known, the next generation is created out of the initial population, based on the dominating subset of design samples. The algorithm continues until the maximum number of iterations is realized. In this work, the population size is fixed at 50 design samples, following a rule of thumb of 10

samples per design parameter [53]. The optimization algorithm is characterized by a crossover and mutation probability of 0.9 and 0.1 respectively.

3. Results and discussion

The UQ and RDO methods are applied to the HRES to determine the optimized designs and to evaluate their performance under the variable market conditions scenario and fixed market conditions scenario. First, the Pareto set of optimized designs is presented, supplemented by a global sensitivity analysis to capture the driving uncertainties. Additionally, the stochastic design performance of these optimized designs is compared based on the Cumulative Distribution Function (CDF).

3.1. Robust Design Optimization and global sensitivity analysis

The RDO method is applied four times independently on the HRES: for the dwelling and community in the fixed market conditions scenario and the variable market conditions scenario. In both scenarios, a trade-off exists between minimizing the LCOE mean and minimizing the LCOE standard deviation for the dwelling (Figure 3) and for the community (Figure 4), which is illustrated by the Pareto set of optimized designs. For each optimized design, the total Sobol' indices of the LCOE and the statistical moments of the corresponding SSR are quantified.

The minimum LCOE mean is achieved by a PV array (e.g. 2.7 $\mathrm{kW_p}$ for the dwelling), which in the variable market conditions scenario induces a slightly larger LCOE standard deviation (e.g. 55.9 €/MWh for the dwelling) than in the fixed market conditions scenario (e.g. 55.1 €/MWh for the dwelling), due to the additional uncertainty present on the PV array investment cost and interest rate (Figure 3 and Figure 4). For this design, the uncertainty related to the grid electricity price (i.e. wholesale electricity price and proportion of the wholesale electricity price in the total charged cost per MWh consumed) dominates the LCOE standard deviation, due to the significant dependency on the grid to

comply with the electricity demand (SSR mean = 30%). To reduce the LCOE standard deviation, at the expense of a minimal increase in LCOE mean, the Pareto set of optimized designs implies to increase the PV array capacity, which consequently increases the SSR mean and therefore decreases the Sobol' indices related to grid electricity. To illustrate for the dwelling, increasing the PV array capacity proves to be a cost-efficient approach (i.e. with minimal increase in LCOE mean) to decrease the LCOE standard deviation down to 48.5 €/MWh in the variable market conditions scenario and down to 42.6 €/MWh in the fixed market conditions scenario. Despite the LCOE standard deviation can be reduced modestly by increasing the PV array capacity, the proposed PV designs remain primarily dependent on grid electricity (SSR mean $< 40\%$) and the envisioned LCOE is therefore subject to a significant standard deviation.

To further decrease the LCOE standard deviation over a higher SSR mean threshold (e.g. SSR mean $> 40\%$ for the community, Figure 4), PV-battery designs are configured by the optimization algorithm, instead of further increasing solely the PV array capacity. This because the SSR mean stagnates over a certain PV capacity threshold, while the inclusion of a battery stack enables to cover part of the demand when insufficient solar irradiance is available. Hence, the optimization algorithm suggests designs which subsequently increase in both PV array capacity and battery stack capacity to further reduce the LCOE standard deviation (and thus increase in SSR mean). For these designs, the LCOE standard deviation is significantly characterized by the uncertainty related to the battery (e.g. total Sobol' index up to 16% in the variable market conditions scenario for the dwelling, Figure 3). Therefore, improving the battery lifetime estimation is considered an effective approach to reduce the LCOE standard deviation of these designs with an external measure.

For the dwelling, a PV-battery configuration defines the robust design which achieves an SSR mean of 54 % in the variable market conditions scenario and an SSR mean of 57 % in the fixed market conditions scenario. Consequently, from this point, improving the SSR mean leads to an increase in LCOE standard deviation due to the significant increase in system capacity, from which

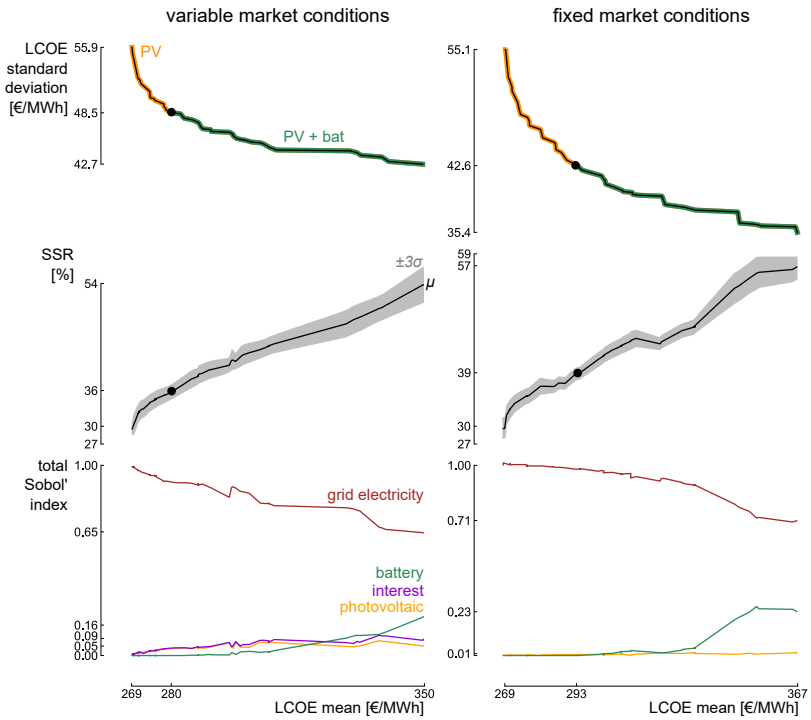

Figure 3: For the dwelling, the Pareto front illustrates that a trade-off exists between minimizing the Levelized Cost Of Electricity (LCOE) mean and LCOE standard deviation. Reducing the LCOE standard deviation cost-efficiently is suggested by subsequently expanding a PV array and battery stack. This system capacity evolution improves the mean Self-Sufficiency Ratio (SSR) and consequently reduces the importance of the grid price uncertainty. Instead, the uncertainty related to the interest rate (in the variable market conditions scenario) and the battery stack gradually gain in importance in the LCOE variation.

the corresponding uncertainty overcompensates the reduction in the uncertainty related to grid electricity. As lower uncertainty is related to the system capacity in the fixed market conditions scenario (i.e. deterministic investment costs), the SSR mean for the robust design in this scenario is higher than for the robust design in the variable market scenario. Therefore, the LCOE standard deviation for the robust design in the fixed market conditions scenario (35.4 €/MWh) is lower than for the robust design characterized in the variable market scenario (42.7 €/MWh). For the community, the robust design includes both a battery stack and a hydrogen-based energy system (Figure 4), despite the large uncer-

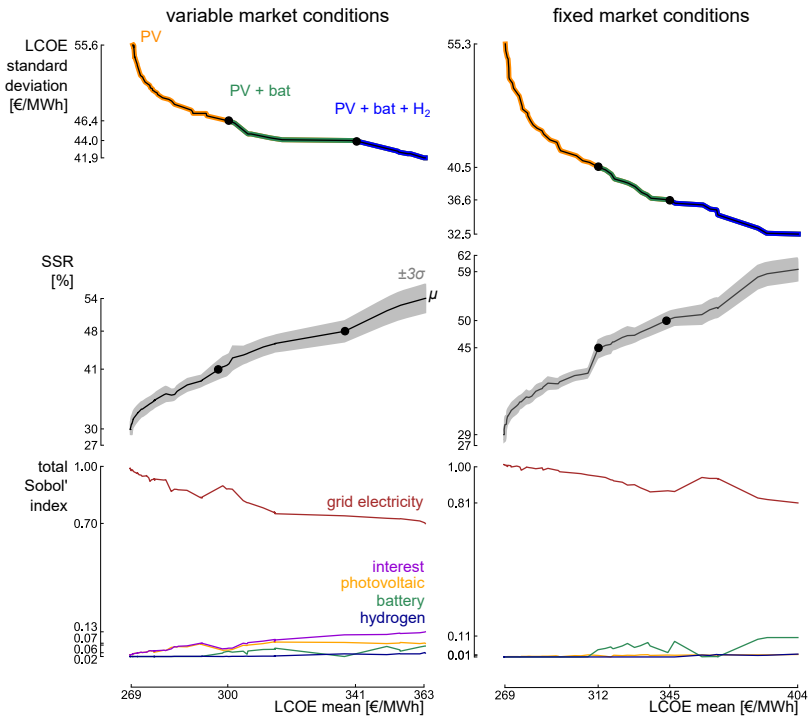

Figure 4: For the community, the Pareto front illustrates that a trade-off exists between minimizing the Levelized Cost Of Electricity (LCOE) mean and LCOE standard deviation. Reducing the LCOE standard deviation cost-efficiently is suggested by subsequently expanding a PV array, battery stack and the hydrogen-based energy system. This system capacity evolution improves the mean Self-Sufficiency Ratio (SSR) and consequently reduces the importance of the grid price uncertainty. Instead, the uncertainty related to the interest rate (in the variable market conditions scenario) and the battery stack gradually gain in importance in the LCOE variation.

tainty related to the specific cost of the electrolyzer and fuel cell (e.g. $\sigma_{\mathrm{CAPEX_{elec}}}$ = 202 €/kW as opposed to $\sigma_{\mathrm{CAPEX_{bat}}}$ = 73 €/kWh). The decoupling of power (i.e. electrolyzer and fuel cell) and energy (i.e. hydrogen tank, $\sigma_{\mathrm{CAPEX_{tank}}}$ = 1.2 €/kWh) enables to curb the uncertainty related to the hydrogen-based energy system present in the LCOE standard deviation. Moreover, this flexible capacity setting of hydrogen storage results in the fact that the significant amount of energy stored over a longer period can be achieved by solely increasing the capacity of the hydrogen tank, as opposed to sizing the entire battery stack

for long-term energy storage. Conclusively, a PV-battery-hydrogen design provides a cost-efficient alternative for a large battery stack at moderate SSR and is therefore configured as a robust alternative in both scenarios for the community.

Table 1: The characteristics of the three evaluated optimized designs for the dwelling: a PV design and a PV-battery design that achieve the lowest LCOE mean among their corresponding category and the PV-battery robust design that achieves the lowest LCOE standard deviation.

	N_{PV}	N_{bat}	μ_{LCOE}	σ_{LCOE}	μ_{SSR}
	$\mathrm{kW_p}$	kWh	€/MWh	€/MWh	%
variable market scenario					
PV	2.7		269	55.9	30
PV + bat	5.1	1.0	280	48.5	36
PV + bat robust	5.2	6.9	350	42.7	54
fixed market scenario					
PV	2.7		269	55.1	30
PV + bat	6.9	1.1	293	42.6	39
PV + bat robust	9.1	5.8	367	35.4	57

Table 2: The characteristics of the three evaluated optimized designs for the community: a PV design and a PV-battery design that achieve the lowest LCOE mean among their corresponding category and the PV-battery-hydrogen robust design that achieves the lowest LCOE standard deviation.

	N_{PV}	N_{bat}	N_{ELEC}	N_{FC}	N_{tank}	μ_{LCOE}	σ_{LCOE}	μ_{SSR}
	$\mathrm{MW_p}$	MWh	MW	MW	MWh	€/MWh	€/MWh	%
variable market scenario								
PV	6.9					269	55.6	30
PV + bat	11.6	6.1				300	46.4	41
PV + bat + H_2	16.3	7.1	1.7	0.5	16.7	363	41.9	54
fixed market scenario								
PV	6.5					269	55.3	29
PV + bat	15.0	6.9				312	40.5	45
PV + bat + H_2	21.2	8.4	2.3	0.5	16.7	404	32.5	59

3.2. Comparison of stochastic performance

Due to the trade-off between minimizing the LCOE mean and minimizing the LCOE standard deviation, each design out of the Pareto set of optimized designs carries an advantage in either average performance or robustness. To evaluate the overall stochastic performance, the CDF is constructed for three representative optimized designs: the PV design that achieves the lowest LCOE mean, the PV-battery design that achieves the lowest LCOE mean among the proposed PV-battery designs and a robust design, which corresponds to the lowest LCOE standard deviation for the dwelling (Table 1) and for the community (Table 2). Among these designs, the PV design achieves the highest probability that in reality, the resulting LCOE over the lifetime will be lower than any predefined LCOE upper limit for the dwelling and community (yellow CDF in Figure 5 and Figure 6, respectively). To illustrate in a variable market conditions scenario, if the dwelling owner predefines an LCOE upper limit of 250 €/MWh to ensure an affordable cost of electricity, the PV design provides a probability of 44 % that the LCOE in reality will be below or equal to that upper limit. Alternatively, a lower probability that the real LCOE will be below this upper limit is achieved by the PV-battery design (33 %) and by full grid-dependency (24 %). However, when the upper limit value is determined higher or equal to 350 €/MWh in the variable market conditions scenario (374 €/MWh in the fixed market conditions scenario), the PV-battery design achieves a similar probability of resulting in an LCOE below the upper limit as the PV design. This observation is explained by the lower LCOE standard deviation of the PV-battery design, which steepens the corresponding CDF and therefore realises the intersection between the PV and PV-battery CDF, despite the larger LCOE mean of the PV-battery design.

The PV design achieves a rather low SSR mean (30 %), which makes this design vulnerable to grid behavior, fluctuating electricity prices and potential power cuts. Moreover, operating over a higher SSR threshold reduces the risk of black-out, as it avoids the simultaneous power extraction from the grid of different demand types. Therefore, the PV-battery design and robust design are of interest when operating over a larger SSR threshold is preferred (Figure 7 for

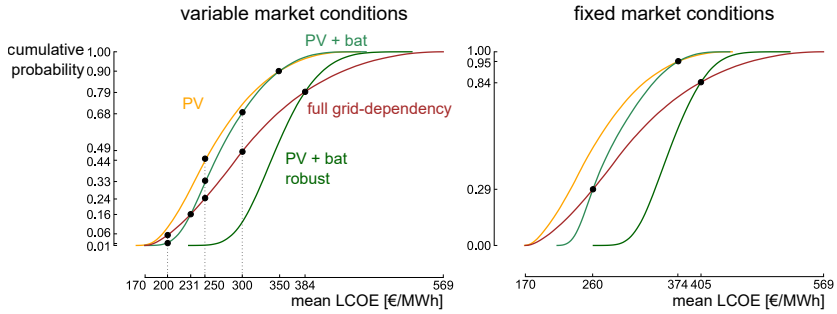

Figure 5: The Cumulative Density Functions (CDF) of three optimized designs and full grid-dependency for the dwelling. The intersection point between two CDFs illustrates the minimum LCOE upper limit that has to be defined, in order for the optimized design to achieve a higher probability than full grid-dependency to achieve an LCOE below this upper limit in reality.

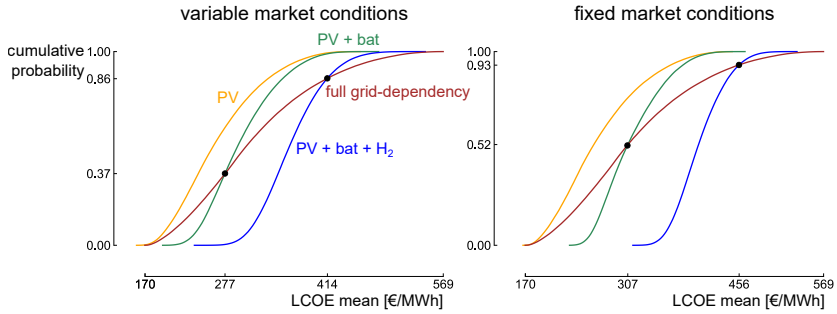

Figure 6: The Cumulative Density Functions (CDF) of three optimized designs and full grid-dependency for the community. The intersection point between two CDFs illustrates the minimum LCOE upper limit that has to be defined, in order for the optimized design to achieve a higher probability than full grid-dependency to achieve an LCOE below this upper limit in reality.

the dwelling and Figure 8 for the community). To illustrate for the dwelling in a variable market scenario, the PV-battery design with the lowest LCOE mean achieves an SSR mean of 36 %, while the robust PV-battery design achieves an SSR mean of 54 %.

When operating over a higher SSR threshold is considered, the performance of the PV-battery design (green CDF in Figure 5 and Figure 6) is of interest and can be compared with full grid-dependency (red CDF in Figure 5 and Figure 6). In this comparison, the preferred design depends on the predefined LCOE upper

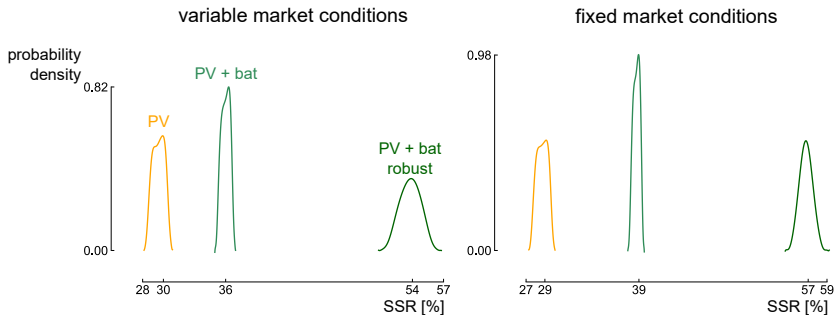

Figure 7: For the dwelling, the probability density functions of the SSR for three optimized designs illustrate the different SSR thresholds over which the designs operate.

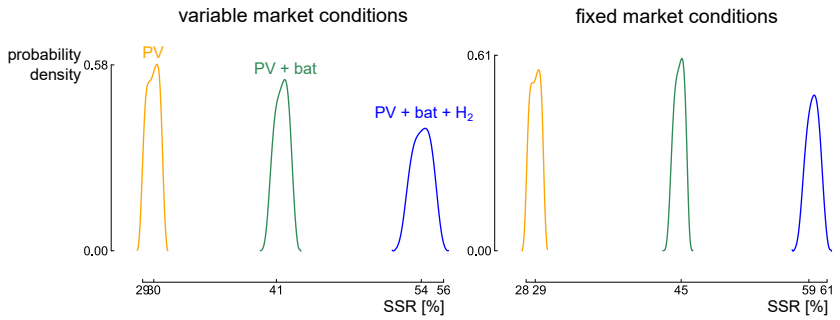

Figure 8: For the community, the probability density functions of the SSR for three optimized designs illustrate the different SSR thresholds over which the designs operate.

limit (and thus on the financial flexibility of the owner). To illustrate for the dwelling in the variable market conditions scenario, both the PV-battery design and full grid-dependency result in a probability of 16 % that the LCOE in reality will be below or equal to 231 €/MWh. If the LCOE upper limit is estimated even lower by the building owner to ensure an affordable cost of electricity, full grid-dependency results in a higher probability of ending up below the upper limit than the PV-battery design: e.g. full grid-dependency achieves a probability of 6 % that the LCOE in reality will be below 200 €/MWh, while the PV-battery design ensures a probability of only 1 %. Instead, if the LCOE upper limit is set higher than 231 €/MWh, the PV-battery design ensures a higher probability: e.g. full grid-dependency results in a probability of 49 % that the LCOE in reality will be below or equal to 300 €/MWh, while the PV-battery design ensures a

probability of 68 %. Conclusively, when the household projects an LCOE of at least 231 €/MWh as a maximum to ensure an affordable cost of electricity, the PV-battery design provides a higher probability of complying with this upper limit than full grid-dependency. Similar results are presented for the community.

Despite the lowest LCOE standard deviation, the CDF of the robust designs do not intersect with the other evaluated optimized designs and is therefore only of interest when operating over a larger SSR threshold. If so, then the robust PV-battery design for the dwelling (dark green CDF in Figure 5) proves to be beneficial over full grid-dependency when the LCOE upper limit is set above 384 €/MWh in the variable market conditions scenario and above 405 €/MWh in the fixed market conditions scenario. For the community, a PV-battery-hydrogen configuration is characterized as a robust design (blue CDF in Figure 6). This design is beneficial over full grid-dependency when the LCOE upper limit is defined higher than 414 €/MWh in the variable market conditions scenario and higher than 456 €/MWh in the the fixed market conditions scenario. Consequently, a PV-battery-hydrogen design presents a cost-competitive alternative over full grid-dependency and operates over a significant SSR threshold ($\geq 54\,\%$), which reduces the risk of black-out and power cuts.

4. Conclusion

The robust design optimization method illustrates a trade-off between minimizing the levelized cost of electricity mean and minimizing the standard deviation for a dwelling and a community. A photovoltaic array achieves the lowest levelized cost of electricity mean (i.e. 269 €/MWh). Additionally, such a system ensures the highest probability that the levelized cost of electricity in reality will be below an upper limit, which has been predicted by the system owner to ensure an affordable cost of electricity. Nevertheless, the proposed photovoltaic arrays remain primarily dependent on grid electricity ($self - sufficiency\ ratio\ mean \approx 30\%$) and therefore subject to a significant standard deviation, risk of black-out and power cuts.

Photovoltaic-battery designs reduce this grid-dependency by increasing the self-sufficiency ratio and therefore decrease the levelized cost of electricity standard deviation. When operating over a higher self-sufficiency ratio is of interest, these photovoltaic-battery designs can ensure a higher probability than full grid-dependency to operate below the maximum affordable levelized cost of electricity predicted (e.g. 231 €/MWh for a dwelling in a variable market scenario).

For a community, the robust design achieves a significant self-sufficiency ratio ($\geq 54\,\%$) and includes both a battery stack and a hydrogen-based energy system. This design is least-sensitive to real-life uncertainty as the decoupling of hydrogen power and hydrogen energy enables to curb the contribution of the uncertainty related to the electrolyzer and fuel cell in the levelized cost of electricity uncertainty. Moreover, these designs prove beneficial over full grid-dependency when the maximum allowed levelized cost of electricity is determined above 414 €/MWh in the fixed market conditions scenario and above 456 €/MWh in the variable market conditions scenario. Conclusively, depending on the financial flexibility of the system owner, battery and hydrogen storage provide a higher probability of realizing a levelized cost of electricity below the maximum allowed levelized cost of electricity to ensure affordability than full-grid dependency. Future work will focus on the integration of different locations. Moreover, a heat demand will be included, to fully exploit the fuel cell capability.

5. Acknowledgements

The first author acknowledges the support of Fonds de la Recherche Scientifique - FNRS [35484777 FRIA-B2].

References

[1] F. Birol, Renewables 2018: Market analysis and forecast from 2018 to 2023, Tech. rep., International Energy Agency (2018).

[2] M. Aneke, M. Wang, Energy storage technologies and real life applications–A state of the art review, Applied Energy 179 (2016) 350–377.

[3] Y. Zhang, P. E. Campana, A. Lundblad, J. Yan, Comparative study of hydrogen storage and battery storage in grid connected photovoltaic system: Storage sizing and rule-based operation, Applied Energy 201 (2017) 397–411.

[4] T. Taner, S. A. H. Naqvi, M. Ozkaymak, Techno-economic analysis of a more efficient hydrogen generation system prototype: a case study of PEM electrolyzer with Cr-C coated SS304 bipolar plates, Fuel Cells 19 (2019) 19–26.

[5] A. Buttler, H. Spliethoff, Current status of water electrolysis for energy storage, grid balancing and sector coupling via power-to-gas and power-to-liquids: A review, Renewable and Sustainable Energy Reviews 82 (2018) 2440–2454.

[6] T. Taner, Energy and exergy analyze of PEM fuel cell: a case study of modeling and simulations, Energy 143 (2018) 284–294.

[7] W. Saeed, G. Warkozek, Modeling and analysis of renewable PEM fuel cell system, Energy Procedia 74 (2015) 87–101.

[8] R. Zahedi, M. M. Ardehali, Power management for storage mechanisms including battery, supercapacitor, and hydrogen of autonomous hybrid green power system utilizing multiple optimally-designed fuzzy logic controllers, Energy 204 (2020) 117935.

[9] Y. Han, H. Yang, Q. Li, W. Chen, F. Zare, J. M. Guerrero, Mode-triggered droop method for the decentralized energy management of an islanded hybrid PV/hydrogen/battery DC microgrid, Energy 199 (2020) 117441.

[10] A. Khiareddine, C. B. Salah, D. Rekioua, M. F. Mimouni, Sizing methodology for hybrid photovoltaic/wind/hydrogen/battery integrated to energy management strategy for pumping system, Energy 153 (2018) 743–762.

[11] W. Zhang, A. Maleki, M. A. Rosen, J. Liu, Optimization with a simulated annealing algorithm of a hybrid system for renewable energy including battery and hydrogen storage, Energy 163 (2018) 191–207.

[12] D. Parra, G. S. Walker, M. Gillott, Modeling of PV generation, battery and hydrogen storage to investigate the benefits of energy storage for single dwelling, Sustainable Cities and Society 10 (2014) 1–10.

[13] M. A. Pellow, C. J. Emmott, C. J. Barnhart, S. M. Benson, Hydrogen or batteries for grid storage? A net energy analysis, Energy & Environmental Science 8 (2015) 1938–1952.

[14] E. L. Eriksson, E. M. A. Gray, Optimization and integration of hybrid renewable energy hydrogen fuel cell energy systems A critical review, Applied Energy 202 (2017) 348–364.

[15] G. Mavromatidis, K. Orehounig, J. Carmeliet, A review of uncertainty characterisation approaches for the optimal design of distributed energy systems, Renewable and Sustainable Energy Reviews 88 (2018) 258–277.

[16] D. Bezmalinović, F. Barbir, I. Tolj, Techno-economic analysis of PEM fuel cells role in photovoltaic-based systems for the remote base stations, International Journal of Hydrogen Energy 38 (2013) 417–425.

[17] A. Younesi, H. Shayeghi, A. Safari, P. Siano, Assessing the resilience of multi microgrid based widespread power systems against natural disasters using Monte Carlo Simulation, Energy 207 (2020) 118220.

[18] Z. Deng, X. Hu, X. Lin, Y. Che, L. Xu, W. Guo, Data-driven state of charge estimation for lithium-ion battery packs based on Gaussian process regression, Energy 205 (2020) 118000.

[19] L. Daróczy, G. Janiga, D. Thévenin, Analysis of the performance of a H-Darrieus rotor under uncertainty using Polynomial Chaos Expansion, Energy 113 (2016) 399–412.

[20] K. Verleysen, D. Coppitters, A. Parente, W. De Paepe, F. Contino, How can power-to-ammonia be robust? Optimization of an ammonia synthesis plant powered by a wind turbine considering operational uncertainties, Fuel 266 (2020) 117049.

[21] J. Shangguan, H. Guo, M. Yue, Robust energy management of plug-in hybrid electric bus considering the uncertainties of driving cycles and vehicle mass, Energy 203 (2020) 117836.

[22] F. S. Gazijahani, J. Salehi, Reliability constrained two-stage optimization of multiple renewable-based microgrids incorporating critical energy peak pricing demand response program using robust optimization approach, Energy 161 (2018) 999–1015.

[23] D. Coppitters, W. De Paepe, F. Contino, Surrogate-assisted robust design optimization and global sensitivity analysis of a directly coupled photovoltaic-electrolyzer system under techno-economic uncertainty, Applied Energy 248 (2019) 310–320.

[24] N. Rezaei, A. Khazali, M. Mazidi, A. Ahmadi, Economic energy and reserve management of renewable-based microgrids in the presence of electric vehicle aggregators: A robust optimization approach, Energy 201 (2020) 117629.

[25] K. Akbari, M. M. Nasiri, F. Jolai, S. F. Ghaderi, Optimal investment and unit sizing of distributed energy systems under uncertainty: A robust optimization approach, Energy and Buildings 85 (2014) 275–286.

[26] A. Parisio, C. Del Vecchio, A. Vaccaro, A robust optimization approach to energy hub management, International Journal of Electrical Power & Energy Systems 42 (2012) 98–104.

[27] S. Abraham, M. Raisee, G. Ghorbaniasl, F. Contino, C. Lacor, A robust and efficient stepwise regression method for building sparse polynomial chaos expansions, Journal of Computational Physics 332 (2017) 461–474.

[28] M. Castañeda, A. Cano, F. Jurado, H. Sánchez, L. M. Fernández, Sizing optimization, dynamic modeling and energy management strategies of a stand-alone PV/hydrogen/battery-based hybrid system, International Journal of Hydrogen Energy 38 (2013) 3830–3845.

[29] W. F. Holmgren, C. W. Hansen, M. A. Mikofski, pvlib python: a python package for modeling solar energy systems, The Journal of Open Source Software 3 (2018) 884.

[30] W. De Soto, S. A. Klein, W. A. Beckman, Improvement and validation of a model for photovoltaic array performance, Solar Energy 80 (2006) 78–88.

[31] G. de Oliveira e Silva, P. Hendrick, Leadacid batteries coupled with photovoltaics for increased electricity self-sufficiency in households, Applied Energy 178 (2016) 856–867.

[32] S. Blaifi, S. Moulahoum, I. Colak, W. Merrouche, An enhanced dynamic model of battery using genetic algorithm suitable for photovoltaic applications, Applied Energy 169 (2016) 888–898.

[33] B. Zakeri, S. Syri, Electrical energy storage systems: A comparative life cycle cost analysis, Renewable and Sustainable Energy Reviews 42 (2015) 569–596.

[34] B. Battke, T. S. Schmidt, D. Grosspietsch, V. H. Hoffmann, A review and probabilistic model of lifecycle costs of stationary batteries in multiple applications, Renewable and Sustainable Energy Reviews 25 (2013) 240–250.

[35] G. Díaz, J. Gómez-Aleixandre, J. Coto, O. Conejero, Maximum income resulting from energy arbitrage by battery systems subject to cycle aging and price uncertainty from a dynamic programming perspective, Energy 156 (2018) 647–660.

[36] C. Phurailatpam, B. S. Rajpurohit, L. Wang, Planning and optimization of autonomous DC microgrids for rural and urban applications in India, Renewable and Sustainable Energy Reviews 82 (2018) 194–204.

[37] I. Pawel, The cost of storage - How to calculate the levelized cost of stored energy (LCOE) and applications to renewable energy generation, Energy Procedia 46 (2014) 68–77.

[38] P. Komor, J. Glassmire, Electricity storage and renewables for island power: a guide for decision makers, Tech. rep., International Renewable Energy Agency (IRENA) (2012).

[39] Z. Abdin, C. J. Webb, E. M. Gray, Modelling and simulation of a proton exchange membrane (PEM) electrolyser cell, International Journal of Hydrogen Energy 40 (2015) 13243–13257.

[40] H. Görgün, Dynamic modelling of a proton exchange membrane (PEM) electrolyzer, International Journal of Hydrogen Energy 31 (2006) 29–38.

[41] K. Murugesan, V. Senniappan, Investigation of water management dynamics on the performance of a Ballard-Mark-V proton exchange membrane fuel cell stack system, International Journal of Electrochemical Science 8 (2013) 7885–7904.

[42] K. Ameur, A. Hadjaissa, M. Ait Cheikh, A. Cheknane, N. Essounbouli, Fuzzy energy management of hybrid renewable power system with the aim to extend component lifetime, International Journal of Energy Research 41 (2017) 1867–1879.

[43] M. Taghvaee, M. Radzi, S. Moosavain, H. Hizam, M. H. Marhaban, A current and future study on non-isolated DC–DC converters for photovoltaic applications, Renewable and sustainable energy reviews 17 (2013) 216–227.

[44] G. A. Rampinelli, A. Krenzinger, F. Chenlo Romero, Mathematical models for efficiency of inverters used in grid connected photovoltaic systems, Renewable and Sustainable Energy Reviews 34 (2014) 578–587.

[45] S. Wilcox, W. Marion, Users manual for TMY3 data sets, Tech. rep., National Renewable Energy Laboratory Golden, CO (2008).

[46] Open Energy Information, Commercial and Residential Hourly Load Profiles for all TMY3 Locations in the United States, Available online: http://en.openei.org/datasets/dataset/commercial-and-residential-hourly-load-profiles-for-all-tmy3-\locations-in-the-united-states. Accessed: 16th February 2019.

[47] M. Montero Carrero, I. R. Sánchez, W. D. Paepe, A. Parente, F. Contino, Is There a Future for Small-Scale Cogeneration in Europe ? Economic and Policy Analysis of the Internal Humid Air Turbine Cycles, Energies 12 (2019) 1–27.

[48] P. Balcombe, D. Rigby, A. Azapagic, Investigating the importance of motivations and barriers related to microgeneration uptake in the UK, Applied Energy 130 (2014) 403–418.

[49] Elia, Electricity scenarios for Belgium towards 2050: Elia's quantified study on the energy transition in 2030 and 2040, Tech. rep., Elia (2017).

[50] B. Sudret, Polynomial chaos expansions and stochastic finite-element methods, Risk and Reliability in Geotechnical Engineering Chap. 6 (2014) 265–300.

[51] W. De Paepe, D. Coppitters, S. Abraham, P. Tsirikoglou, G. Ghorbaniasl, F. Contino, Robust Operational Optimization of a Typical micro Gas Turbine, Energy Procedia 158 (2019) 5795–5803.

[52] S. Giorgetti, D. Coppitters, F. Contino, W. D. Paepe, L. Bricteux, G. Aversano, A. Parente, Surrogate-Assisted Modeling and Robust Optimization of a Micro Gas Turbine Plant With Carbon Capture, Journal of Engineering for Gas Turbines and Power 142.

[53] P. Tsirikoglou, S. Abraham, F. Contino, Ö. Bağci, J. Vierendeels, G. Ghorbaniasl, Comparison of metaheuristics algorithms on robust design opti-

mization of a plain-fin-tube heat exchanger, in: 18th AIAA/ISSMO Multidisciplinary Analysis and Optimization Conference, 2017, p. 3827.

[54] S. M. Wilcox, National solar radiation database 1991-2010 update: User's manual, Tech. rep., National Renewable Energy Lab.(NREL), Golden, CO (United States) (2012).

[55] Sunpower, X-Series residential solar panels: supplementary technical specifications.

[56] N. Lukač, S. Seme, K. Dežan, B. Žalik, G. Štumberger, Economic and environmental assessment of rooftops regarding suitability for photovoltaic systems installation based on remote sensing data, Energy 107 (2016) 854–865.

[57] L. Reichenberg, F. Hedenus, M. Odenberger, F. Johnsson, The marginal system LCOE of variable renewables Evaluating high penetration levels of wind and solar in Europe, Energy 152 (2018) 914–924.

[58] B. Guinot, B. Champel, F. Montignac, E. Lemaire, D. Vannucci, S. Sailler, Y. Bultel, Techno-economic study of a PV-hydrogen-battery hybrid system for off-grid power supply: Impact of performances' ageing on optimal system sizing and competitiveness, International Journal of Hydrogen Energy 40 (2015) 623–632.

[59] W. G. Colella, B. D. James, J. M. Moton, G. Saur, T. Ramsden, Techno-economic Analysis of PEM Electrolysis for Hydrogen Production, Tech. rep., Strategic Analysis inc. and National Renewable Energy Laboratory (NREL) (2014).

[60] L. Placca, R. Kouta, J. F. Blachot, W. Charon, Effects of temperature uncertainty on the performance of a degrading PEM fuel cell model, Journal of Power Sources 194 (2009) 313–327.

[61] T. Taner, Energy and exergy analyze of PEM fuel cell: A case study of modeling and simulations, Energy 143 (2018) 284–294.

[62] S. Niaz, T. Manzoor, A. H. Pandith, Hydrogen storage: Materials, methods and perspectives, Renewable and Sustainable Energy Reviews 50 (2015) 457–469.

[63] Y. Budak, Y. Devrim, Comparative study of PV/PEM fuel cell hybrid energy system based on methanol and water electrolysis, Energy conversion and management 179 (2019) 46–57.

[64] E. Ozden, I. Tari, PEM fuel cell degradation effects on the performance of a stand-alone solar energy system, International Journal of Hydrogen Energy 42 (2017) 13217–13225.

[65] J. Kotowicz, D. Wecel, M. Jurczyk, Analysis of component operation in power-to-gas-to-power installations, Applied energy 216 (2018) 45–59.

[66] J. Wu, X. Z. Yuan, J. J. Martin, H. Wang, J. Zhang, J. Shen, S. Wu, W. Merida, A review of pem fuel cell durability: Degradation mechanisms and mitigation strategies, Journal of Power Sources 184 (2008) 104–119.

[67] F. Abbasi, M. Abapour, Reliability and cost optimization of multi-input bidirectional DC/DC converter implemented in renewable sources, Majlesi Journal of Electrical Engineering 12 (2018) 57–65.

[68] A. Allouhi, M. S. Buker, H. El-houari, A. Boharb, M. Benzakour Amine, T. Kousksou, A. Jamil, PV water pumping systems for domestic uses in remote areas: Sizing process, simulation and economic evaluation, Renewable Energy 132 (2019) 798–812.

[69] A. Kashefi Kaviani, G. H. Riahy, S. M. Kouhsari, Optimal design of a reliable hydrogen-based stand-alone wind/PV generating system, considering component outages, Renewable Energy 34 (2009) 2380–2390.

[70] M. A. Ramli, A. Hiendro, S. Twaha, Economic analysis of PV/diesel hybrid system with flywheel energy storage, Renewable Energy 78 (2015) 398–405.

[71] Vlaamse Regulator van de Elektriciteits- en Gasmarkt (Flemish Regulator of the Electricity and Gas Market), Evolution of the household electricity bill, Available online: https://infogram.com/evolutie-energiefactuur-gezin-1h7j4djlx9k94nr?live. Accessed: 3th February 2020.

[72] Triami Media BV, Historic inflation Belgium - CPI inflation, Available online: inflation.eu/inflation-rates/belgium/historic-inflation/cpi-inflation-belgium.aspx. Accessed: 1st August 2019 (2019).

[73] T. H. T. Nguyen, T. Nakayama, M. Ishida, Optimal capacity design of battery and hydrogen system for the DC grid with photovoltaic power generation based on the rapid estimation of grid dependency, International Journal of Electrical Power & Energy Systems 89 (2017) 27–39.

[74] A. Singh, P. Baredar, B. Gupta, Techno-economic feasibility analysis of hydrogen fuel cell and solar photovoltaic hybrid renewable energy system for academic research building, Energy Conversion and Management 145 (2017) 398–414.

Appendix A. Additional data and figure

parameter, unit	min	max	Ref.
photovoltaic			
G, %	-9.9	+7.7	[54]
T_{amb}, K	-0.9	+0.9	[54]
power tolerance$_{\mathrm{PV}}$, %	0	5	[55]
CAPEX$_{\mathrm{PV}}$, €/kW$_{\mathrm{p}}$	430	780	[56]
OPEX$_{\mathrm{PV}}$, €/kW$_{\mathrm{p}}$	16	19	[57]
hydrogen			
CAPEX$_{\mathrm{elec}}$, €/kW	1400	2100	[5]
OPEX$_{\mathrm{elec}}$, % of CAPEX$_{\mathrm{elec}}$	3	5	[5]
$R_{\mathrm{c,elec}}$, % of CAPEX$_{\mathrm{elec}}$	15	20	[58, 59]
n_{elec}, kh	60	100	[5]
T_{elec}, K	347	359	[60]
p_{elec}, bar	-0.1	0.1	[61]
degradation$_{\mathrm{elec}}$, µV/h	4	8	[5]
CAPEX$_{\mathrm{tank}}$, €/kWh	10.4	14.4	[62]
OPEX$_{\mathrm{tank}}$, % of CAPEX$_{\mathrm{tank}}$	1	2	[3, 58]
CAPEX$_{\mathrm{FC}}$, €/kW	1500	2400	[63–65]
OPEX$_{\mathrm{FC}}$, €/h	0.045	0.135	[63, 64]
$R_{\mathrm{c,FC}}$, % of CAPEX$_{\mathrm{FC}}$	25	30	[63, 64]
n_{FC}, kh	20	30	[3, 34]
T_{FC}, K	347	359	[60]
p_{FC}, bar	-0.1	0.1	[61]
degradation$_{\mathrm{FC}}$, µV/h	2	10	[66]
battery			
CAPEX$_{\mathrm{bat}}$, €/kWh	102	354	[34]
OPEX$_{\mathrm{bat}}$, €/kWh	15	28	[33, 34]

$R_{\mathrm{c,bat}}$, €/kWh	61	141	[33, 34]
n_{bat}, cycles	500	2000	[34]
self discharge$_{\mathrm{bat}}$, %/day	0.1	0.3	[33]
degradation$_{\mathrm{bat}}$, %/year	3.5	4.0	[37]
converter/inverter			
CAPEX$_{\mathrm{DCDC}}$, €/kW	100	200	[67, 68]
OPEX$_{\mathrm{DCDC}}$, % of CAPEX$_{\mathrm{DCDC}}$	1	5	[69, 70]
CAPEX$_{\mathrm{DCAC}}$, €/kW	342	519	[56]
OPEX$_{\mathrm{DCAC}}$, % of CAPEX$_{\mathrm{DCAC}}$	1	5	[69, 70]
other			
E_{load}, %	+2	+7	[49]
w, €/MWh	46	97	[49]
f_w, %	20	40	[71]
f, %	1	3	[72]
i', %	4	8	[10, 73, 74]

Table A.3: The ranges for the stochastic parameters, used in the Robust Design Optimization (RDO) process.

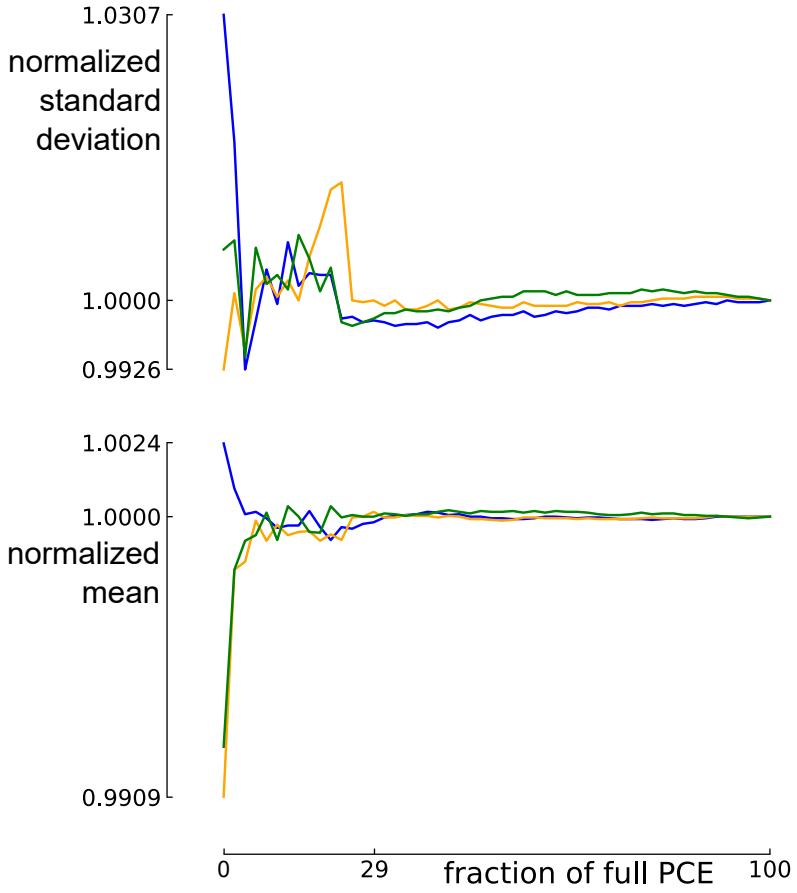

Figure A.9: The gradual increase of the initial number of real model evaluations for 3 design samples illustrates that accurate statistical moments can be acquired by evaluating only 29 % of the required full PCE model evaluations.